



Article

Mutual Inductance Identification and Bilateral Cooperation Control Strategy for MCR-BE System

Ke Li ¹, Yuanmeng Liu ¹, Xiaodong Sun ^{2,*}  and Xiang Tian ^{2,*}

¹ School of Electrical and Information Engineering, Jiangsu University, Zhenjiang 212013, China; like@ujs.edu.cn (K.L.); 2222107120@stmail.ujs.edu.cn (Y.L.)

² Automotive Engineering Research Institute, Jiangsu University, Zhenjiang 212013, China

* Correspondence: xdsun@ujs.edu.cn (X.S.); tianxiangsky@ujs.edu.cn (X.T.); Tel.: +86-0511-8878-2845 (X.S.)

Abstract: Considering that the excitation method of an electric excitation synchronous motor has the disadvantages of the brush and slip ring, this article proposes a new brushless excitation system, which includes two parts: a wireless charging system and a motor. To meet the requirements of maximum transmission efficiency and constant voltage output of the system, a bilateral cooperation control strategy is proposed. For the strategy, the buck converter in the receiving side of the system can maintain maximum transmission efficiency through impedance matching, while the inverter in the transmitting side can keep the output voltage constant through phase shift modulation. In the control process, considering that the offset of coupling coils will affect the control results, a grey wolf optimization–particle swarm optimization algorithm is proposed to identify mutual inductance. Simulation and experimental results show that this identification algorithm can improve the identification accuracy and maximize the avoidance of falling into local optima. The final experimental result shows that the bilateral cooperation control strategy can maintain the output voltage around 48 V and the transmission efficiency around 84.5%, which meets the expected requirements.

Keywords: brushless excitation system; grey wolf optimization–particle swarm optimization algorithm; mutual inductance identification; bilateral cooperation control



Citation: Li, K.; Liu, Y.; Sun, X.; Tian, X. Mutual Inductance Identification and Bilateral Cooperation Control Strategy for MCR-BE System. *World Electr. Veh. J.* **2024**, *15*, 196. <https://doi.org/10.3390/wevj15050196>

Academic Editor: Joeri Van Mierlo

Received: 5 March 2024

Revised: 27 April 2024

Accepted: 30 April 2024

Published: 2 May 2024



Copyright: © 2024 by the authors. Licensee MDPI, Basel, Switzerland. This article is an open access article distributed under the terms and conditions of the Creative Commons Attribution (CC BY) license (<https://creativecommons.org/licenses/by/4.0/>).

1. Introduction

Due to the scarcity of global oil resources and environmental pollution caused by carbon emissions [1,2], traditional fuel vehicles are gradually withdrawing from the transportation market, while new energy vehicles that use electricity instead of oil are rapidly developing. New energy vehicles mainly include electric vehicles [3] and hybrid electric vehicles [4,5]. Among them, electric vehicles are gradually occupying the transportation market. The core components of electric vehicles are motors and batteries. Currently, the most popular motors include permanent magnet synchronous motors (PMSMs) [6] and electrically excited synchronous motors (EESMs). The PMSM dominates the automotive market due to its advantages of high torque density and high efficiency [7]. However, due to the high cost of permanent magnet materials, the production cost of PMSM is relatively high. The EESM generates a magnetic field through an external excitation current, which avoids the use of permanent magnets [8,9]. However, the excitation method of the EESM requires a brush and slip ring, which will produce carbon powder during long-term friction. This disadvantage will reduce insulation performance and seriously affect the safe operation of the motor [10]. Therefore, there is an urgent need for brushless excitation technology.

With the development of wireless power transfer (WPT) technology, wireless charging technology has received widespread attention in recent years [11–13]. Based on wireless charging technology, this article proposes a new brushless excitation system by combining

wireless charging technology and a motor. For the system, a coupling coil is installed on each of the stator and rotor. When the stored electrical energy of the battery is transmitted to the stator coil, an alternating magnetic field is generated around the stator. After being affected by the magnetic field, the rotor coil also generates an induced magnetic field, which interacts with the stator magnetic field to generate torque to drive the rotor [14,15]. During this process, there is no need for a brush and slip ring, so the motor achieves brushless excitation, which is called magnetic coupled resonant brushless excitation (MCR-BE) technology.

Due to the poor coupling between the transmitting coil on the ground and the receiving coil of the car in the MCR-BE system, the leakage inductance phenomenon is obvious, and will lead to low charging efficiency of the battery. Therefore, it is necessary to add a resonant compensation topology. Traditional low-order compensation topologies, such as SS and SP [16,17], are susceptible to the influence of circuit component parameters on their output characteristics, while LCC-LCC topology [18] has complex structures and high costs. In recent years, LCC-S topology [19] has become a popular research topic, and the output voltage of the topology is less affected by component parameters, which is beneficial for constant voltage charging. For the charging process, constant voltage charging and maximum charging efficiency is crucially important. However, for the dynamic charging process (i.e., during the driving process of the car), the mutual inductance between the coils will undergo uncertain changes, which will affect the charging efficiency [20,21]. DC-DC conversion is a classic method for achieving efficiency optimization [22]. The authors in reference [23] added a step-down boost converter to the receiving side of the WPT system and adjusted the input voltage on the transmitting side to track the maximum efficiency point. In reference [24], a cascaded boost-buck converter with dual switch control is used on the receiving side, and the maximum efficiency point is tracked through two duty cycles. In reference [25], the buck converter on the receiving side changes the equivalent load by controlling the current on the transmitting side, thereby achieving maximum efficiency tracking.

However, these studies only considered efficiency optimization and ignored constant voltage output. In order to achieve both goals simultaneously, the bilateral cooperation control strategy has become a popular research topic. Reference [26] proposed a collaborative control strategy using a full bridge inverter and a semi-active rectifier, which eliminates the wireless communication link between the two parts and greatly optimizes the system. Reference [27] proposed a collaborative control strategy using a step-down converter and a semi-active rectifier. The semi-active rectifier is used to maintain constant voltage/current output, while the step-down converter is used to find the minimum input power. This strategy achieves maximum transmission efficiency. However, when there is a deviation between coupling coils, these control strategies need to optimize mutual inductance in order to work properly.

Therefore, based on these studies, this article first identifies mutual inductance, and then adopts a bilateral cooperation control strategy to achieve efficiency optimization and constant voltage output. For mutual inductance identification, the authors in [28] proposed a method to identify mutual inductance and load by measuring input voltage and current under the same operating frequency. However, the accuracy of this method decreased when approaching resonance. The authors in [29] developed a system for mutual inductance identification by analyzing the voltage and current of fundamental and harmonics waves, but its calculation process is complex. The authors in [30] proposed a vision-based misalignment detection method, which estimates the mutual inductance by finite element simulation of the relationship between magnetic field position and intensity. However, differences between coil manufacturing and simulation can lead to differences in actual results. This article proposes an improved particle swarm optimization algorithm as the identification algorithm; for the bilateral cooperation control strategy, this article proposes a cooperation control strategy using a buck converter and inverter.

The structure of this article is as follows. Section 2 introduces the working principle and mathematical model of the MCR-BE system. Section 3 introduces the bilateral cooperation control strategy and GWO-PSO algorithm. Section 4 verifies the feasibility of the bilateral collaborative control strategy and GWO-PSO algorithm. Section 5 presents experimental validation.

2. Principle of MCR-BE System

2.1. Structure of MCR-BE System

Figure 1 shows the structural diagram of the MCR-BE system, which consists of a wireless charging system [31,32] and a motor. In the wireless charging system, a transmitting coupling coil is installed below the ground (or road), and a receiving coupling coil is installed in the car chassis. The DC voltage provided by the DC power supply is converted into AC voltage through an inverter device and transmitted to the transmitting coupling coil. Subsequently, this AC voltage forms an alternating magnetic field around the transmitting coil. When the receiving coupling coil is within the magnetic field range, an induced electromotive force is generated inside the coil, which also generates a magnetic field and interacts with the magnetic field of the transmitting coil, thereby generating an AC voltage inside the receiving coil. The AC voltage is converted into DC voltage through a rectifier circuit and ultimately transmitted to the battery. Through two non-contact coupling coils, DC voltage is transmitted from the power source to the battery, thus achieving wireless charging.

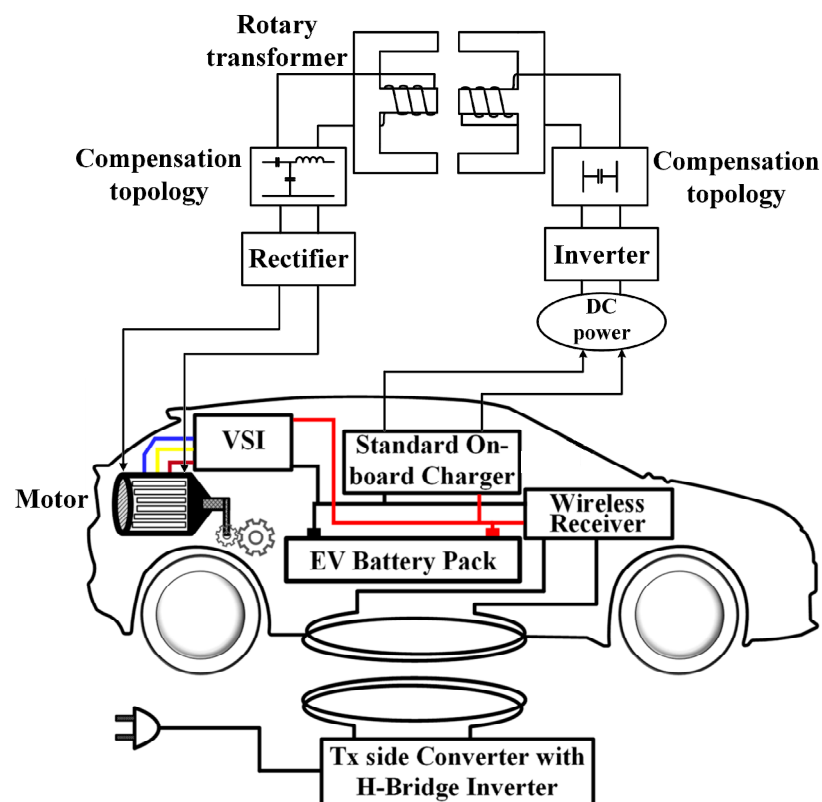


Figure 1. Structure diagram of the MCR-BE system.

The battery transfers the stored electrical energy to the motor to drive the car. During this process, two coupling coils are also installed on the stator and rotor of the motor. The DC voltage provided by the battery is converted into AC voltage through an inverter device and transmitted to the stator coil. Subsequently, this AC voltage forms an alternating magnetic field around the stator coil. When the rotor coil is within the magnetic field range, an induced magnetic field is generated inside it, which interacts with the stator magnetic

field to generate torque to drive the rotor. Through two non-contact coupling coils, DC voltage is transmitted from the stator to the rotor, thus achieving brushless excitation [14,15]. By integrating these two systems, the MCR-BE system is obtained.

The mathematical model of an EESM in a three-phase stationary ABC coordinate system can be expressed as follows.

(1) Mathematical expression of magnetic flux:

$$\psi = Li \quad (1)$$

where ψ , i , and L are the magnetic flux matrix, current matrix, and inductance matrix:

$$\begin{aligned} \psi &= [\psi_A \psi_B \psi_C \psi_f \psi_D \psi_Q]^T \\ i &= [i_A i_B i_C i_f i_D i_Q]^T \\ L &= \begin{bmatrix} L_{AA} & M_{AB} & M_{AC} & M_{Af} & M_{AD} & M_{AQ} \\ M_{BA} & L_{BB} & M_{BC} & M_{Bf} & M_{BD} & M_{BQ} \\ M_{CA} & M_{CB} & L_{CC} & M_{Cf} & M_{CD} & M_{CQ} \\ M_{fA} & M_{fB} & M_{fC} & L_{ff} & M_{fD} & M_{fQ} \\ M_{DA} & M_{DB} & M_{DC} & M_{Df} & L_{DD} & M_{DQ} \\ M_{QA} & M_{QB} & M_{QC} & M_{Qf} & M_{QD} & L_{QQ} \end{bmatrix} \end{aligned} \quad (2)$$

In the inductance matrix, L_{AA} , L_{BB} , and L_{CC} represent the self-inductance of stator A, B, and C three-phase windings, while L_{ff} , L_{DD} , and L_{QQ} represent the self-inductance of rotor excitation winding and damping winding, respectively. The mutual inductance M value of the relevant windings (M_{fQ} , M_{Qf} , M_{DQ} , M_{QD}) that are perpendicular to each other under physical conditions is 0.

(2) Mathematical expression for voltage

The voltage expression of the stator three-phase winding is:

$$\begin{cases} u_A = R_s i_A + \frac{d\psi_A}{dt} \\ u_B = R_s i_B + \frac{d\psi_B}{dt} \\ u_C = R_s i_C + \frac{d\psi_C}{dt} \end{cases} \quad (3)$$

The voltage expressions for the excitation winding and damping winding are:

$$\begin{cases} u_f = R_f i_f + \frac{d\psi_f}{dt} \\ 0 = R_D i_D + \frac{d\psi_D}{dt} \\ 0 = R_Q i_Q + \frac{d\psi_Q}{dt} \end{cases} \quad (4)$$

By integrating Equation (3) and Equation (4) together, the voltage equation for EESM can be obtained as follows:

$$u = Ri + p\psi \quad (5)$$

where p is the differential operator, and u and R are the voltage matrix and resistance matrix, respectively.

2.2. Mathematical Model of LCC-S Topology

Figure 2 shows the structure of the LCC-S topology. The blue arrow represents the equivalent load R_{Leq} , and R_{Leq} represents the equivalent load that R_L reflected before the rectifier circuit. The blue dashed represents the buck converter. According to the characteristics of the rectifier circuit and the buck converter, the relationship between R_{Leq} and R_L can be expressed as:

$$R_{Leq} = \frac{8}{\pi^2 D^2} R_L \quad (6)$$

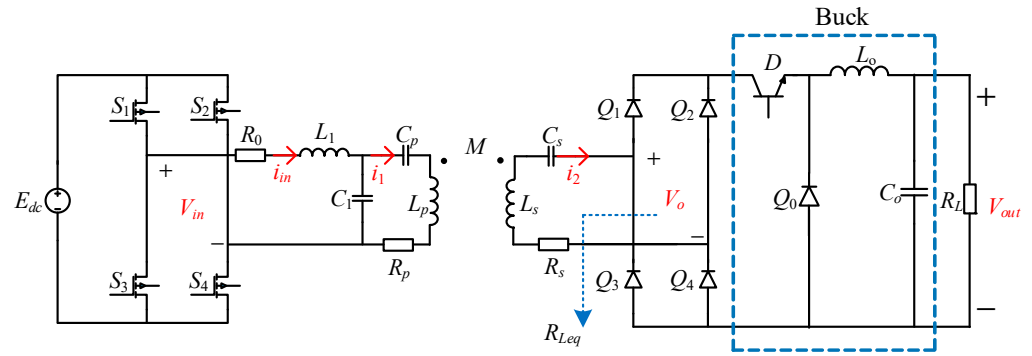


Figure 2. Principle diagram of the wireless charging system.

When L_1 and C_1 are in resonance (resonance frequency named ω_1), C_1 , C_p and L_p are in resonance (resonance frequency named ω_2), L_s and C_s are in resonance (resonance frequency named ω_3), and ω_1 , ω_2 , and ω_3 are equal to the system operation frequency ω , the system is in a completely resonant state. At this time, η can reach its maximum value. Therefore, this article applies resonance state to the LCC-S topology, and ω can be expressed as:

$$\omega = \sqrt{\frac{1}{L_1 C_1}} = \sqrt{\frac{C_1 + C_p}{C_1 C_p L_p}} = \sqrt{\frac{1}{L_s C_s}} \quad (7)$$

When the entire system is in a resonant state, the equivalent impedance Z_2 of the receiving side can be expressed as:

$$Z_2 = R_s + R_{Leq} + j\omega L_s + \frac{1}{j\omega C_s} = R_s + R_{Leq} \quad (8)$$

The equivalent circuit of the receiving side is reflected to the transmitting side, and the reflected impedance Z_r can be expressed as:

$$Z_r = \frac{\omega^2 M^2}{Z_2} = \frac{\omega^2 M^2}{R_s + R_{Leq}} \quad (9)$$

The overall input impedance of the system Z_{in} can be expressed as:

$$Z_{in} = \frac{V_{in}}{i_{in}} = R_0 + j\omega L_1 + \frac{1/j\omega C_1(1/j\omega C_p + j\omega L_p + Z_r + R_p)}{1/j\omega C_1 + 1/j\omega C_p + j\omega L_p + Z_r + R_p} \quad (10)$$

i_{in} , i_1 , and i_2 can be expressed as:

$$\begin{cases} i_{in} = \frac{V_{in}}{Z_{in}} = \frac{V_{in}(\omega^2 M^2 + R_{Leq} R_p + R_p R_s)}{\omega^2 L_1^2 (R_{Leq} + R_s)} \\ i_1 = \frac{i_{in} / j\omega C_1}{1/j\omega C_1 + 1/j\omega C_p + j\omega L_p + Z_r + R_p} = \frac{V_{in}}{j\omega L_1} \\ i_2 = \frac{j\omega M i_1}{Z_2} = \frac{M V_{in}}{(R_{Leq} + R_s) L_1} \end{cases} \quad (11)$$

V_o can be expressed as:

$$V_o = i_2 R_{Leq} = \frac{M V_{in} R_{Leq}}{(R_{Leq} + R_s) L_1} \quad (12)$$

P_{in} can be expressed as:

$$P_{in} = i_{in}^2 R_0 + i_1^2 R_p + i_2^2 (R_s + R_{Leq}) = \frac{V_{in}^2}{R_0 + \frac{\omega^2 L_1^2 (R_{Leq} + R_s)}{\omega^2 M^2 + R_{Leq} R_p + R_p R_s}} \quad (13)$$

P_{out} can be expressed as:

$$P_{out} = i_2^2 R_{Leq} = \frac{\omega^4 L_1^2 M^2 V_{in}^2 R_{Leq}}{[R_0 \omega^2 M^2 + (R_s + R_{Leq})(R_0 R_p + \omega^2 L_1^2)]^2} \tag{14}$$

η can be expressed as:

$$\eta = \frac{\omega^4 L_1^2 M^2 R_{Leq}}{(R_s + R_{Leq})(\omega^4 L_1^2 M^2 + 2\omega^2 M^2 R_0 R_p) + R_0 \omega^4 M^4 + (R_s + R_{Leq})^2 (\omega^2 L_1^2 R_p + R_0 R_p^2)} \tag{15}$$

From Equation (15), it can be seen that η is affected by both M and R_{Leq} . By taking the derivative of the Equation (15) on R_{Leq} and setting it to 0, R_{Leq} can be obtained as:

$$R_{Leq} = R_{\eta max} = \frac{\sqrt{R_p(L_1^2 \omega^2 + R_0 R_p)(\omega^2 M^2 + R_p R_s)(\omega^2 L_1^2 R_s + R_0 \omega^2 M^2 + R_0 R_p R_s)}}{\omega^2 L_1^2 R_p + R_0 R_p^2} \tag{16}$$

When R_{Leq} equals $R_{\eta max}$, η can achieve its maximum value, η_{max} [33].

3. Bilateral Cooperation Control Strategy

3.1. Mutual Inductance Identification

It can be seen from Equation (12) and Equation (15) that mutual inductance M affects transmission efficiency and output voltage. Therefore, it is necessary to identify M . According to Equation (11), the variable factors that affect i_{in} are only R_L and M . Hence, it is reasonable to select the output current of the inverter i_{in} as the model for mutual inductance identification.

The particle swarm optimization algorithm (PSO) is inspired by bird foraging behavior [34,35]. From the principle of PSO, it is reasonable to use this algorithm to determine the mutual inductance of the WPT system at a certain moment; however, conventional PSO has the drawback of easily falling into a local optimum and has a low iteration speed. Considering the above problems, a gray wolf optimization–particle swarm optimization algorithm (GWO-PSO) is proposed to improve its search capability.

In the iterative updating process of GWO, an elite-group guidance strategy is employed, which means selecting the best three individuals in the population for the guided update, instead of relying on the best individual. Moreover, the GWO algorithm adopts a surrounding-guidance strategy, which means that other particles in the search process will surround and approach the elite group [36,37]. Therefore, combining PSO with GWO can further improve the search capability of PSO. The most important search strategy in the GWO algorithm is the surrounding-guidance strategy, and its mathematical model is as follows:

$$\begin{cases} X(t+1) = X_k(t) - A \times D \\ D = |C \times X_k(t) - X(t)| \end{cases} \tag{17}$$

where t represents the iteration number, $X_k(t)$ represents the position vector of prey, and $X(t)$ represents the position vector of gray wolves. Figure 3 shows the surrounding effect:

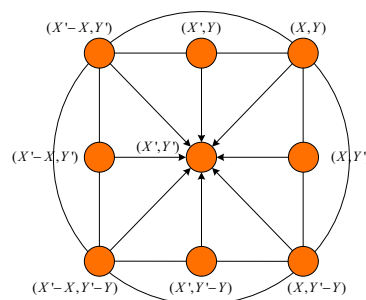


Figure 3. Diagram of wolves surrounding prey.

Assuming the position of the prey is (X', Y') and the position of the gray wolf is (X, Y) , when $\vec{A} = (1, 0), \vec{C} = (1, 1)$, the gray wolf will move to $(X'-X, Y')$ based on the position of the prey. Therefore, when the values of vectors \vec{A} and \vec{C} are different, the surrounding effect can be seen, as shown in Figure 3. \vec{A} and \vec{C} are coefficient vectors with the following meanings:

$$\begin{cases} A = 2pu_1 - p \\ C = 2u_2 \end{cases} \quad (18)$$

where u_1 and u_2 are random numbers in $[0,1]$, and p is a control parameter that linearly decreases in $[0,2]$.

The three elite individuals, the best solution α , suboptimal solution β , and third-best solution δ , can estimate the approximate position of the prey and then lead the entire population to encircle the prey. Combining the elite guidance strategy with the surrounding strategy in Equations (17) and (18), specific formulas can be obtained as follows:

$$\begin{cases} D_\alpha = |C_1 \times X_\alpha(t) - X(t)| \\ D_\beta = |C_1 \times X_\beta(t) - X(t)| \\ D_\delta = |C_1 \times X_\delta(t) - X(t)| \end{cases} \quad (19)$$

where Equation (19) represents the distance of each gray wolf individual to the three best solutions α, β , and δ . The first three equations in Equation (20) represent the directions in which the gray wolf population moves towards the three elite individuals. The fourth equation in Equation (20) represents the update formula of GWO combined with the guidance of the three elite individuals.

$$\begin{cases} X_1(t) = X_\alpha(t) - A_1 \times D_\alpha \\ X_2(t) = X_\beta(t) - A_2 \times D_\beta \\ X_3(t) = X_\delta(t) - A_3 \times D_\delta \\ X(t+1) = \frac{X_1(t)+X_2(t)+X_3(t)}{3} \end{cases} \quad (20)$$

Adding the surrounding update strategy to the updated formula of PSO yields:

$$\begin{cases} v_{i,j}^{t+1} = w(X_{i,j}^t - x_{i,j}^t) + c_1r_1(p_{best\ i,j}^t - x_{i,j}^t) + c_2r_2(g_{best\ j}^t - x_{i,j}^t) \\ x_{i,j}^{t+1} = x_{i,j}^t + v_{i,j}^{t+1} \end{cases} \quad (21)$$

From Equation (21), it can be seen that in the updated process of GWO-PSO, not only are the individual experience and the best particle guidance of PSO retained, but the update strategy of GWO is also introduced. This means that the improved particle swarm optimization algorithm possesses the elite-group guidance strategy and the surrounding-search strategy. By introducing GWO, the drawback of PSO can be overcome. Figure 4 shows the flowchart diagram of GWO-PSO.

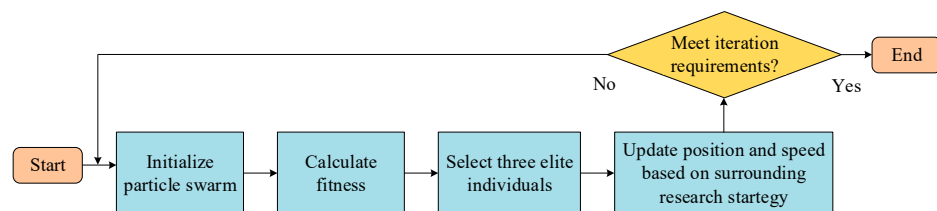


Figure 4. Flowchart diagram of GWO-PSO.

3.2. Bilateral Cooperation Control Strategy

According to Equation (16), it can be inferred that when R_{Leq} equals $R_{\eta\ max}$, the system can achieve η_{max} . However, R_L will change in the process of charging, which will directly

affect R_{Leq} . This article utilizes impedance matching of a buck converter to track $R_{\eta \max}$. If R_{Leq} can track $R_{\eta \max}$ in real-time, then, according to Equation (6), D can be represented as:

$$D = \sqrt{\frac{8R_L}{\pi^2 R_{\eta \max}}} \quad (22)$$

Therefore, by adjusting D , the system can still track the maximum transmission efficiency point even when R_L changes.

Based on Equation (12) and characteristics of the buck converter and rectifier circuit, and the fundamental component effective value of V_{in} [38], V_{out} can be derived as follows (considering that the parasitic internal resistance of the coil is very small, and in order to reduce computational complexity, this article considers both inductance and capacitance as ideal components in subsequent control strategies):

$$V_{out} = \frac{0.9DM}{L_1} \frac{2\sqrt{2}E_{dc}}{\pi} \cos \frac{\theta}{2} \quad (23)$$

In this article, θ is adjusted to maintain a constant output voltage under D variation and M variation.

V_{out} and i_{out} are sampled to determine R_L . Then, the output signal is sent to the transmitting DSP controller through wireless communication. If the output voltage V_{out} is greater than the set voltage V_{ref} , θ will increase; otherwise, θ will decrease. When V_{out} equals V_{ref} , the voltage closed-loop control process can stop. The output equation of the PID controller is:

$$u(t) = K_p e(t) + K_i \sum_{k=0}^n e(t) + K_d [e(t) - e(t-1)] \quad (24)$$

When V_{out} is not equal to V_{ref} , the deviation is input into Equation (24) and compared with a triangular wave to dynamically change θ . The control block diagram of phase shift modulation is shown in Figure 5.

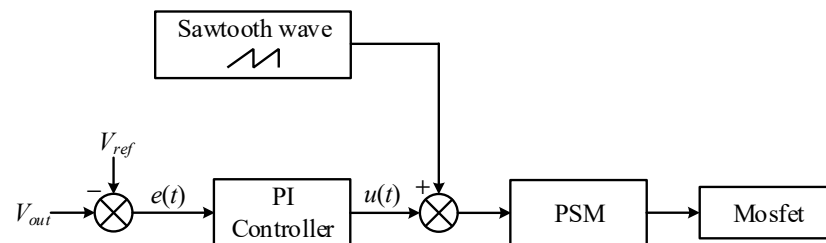


Figure 5. Flowchart of phase shift modulation.

In conclusion, the bilateral cooperation control strategy can be illustrated using Figure 6.

In the control process, the parameters that need to be sampled are output voltage V_{out} , output current i_{out} , and inverter output current i_{in} . The real-time value of the load R_L can be obtained from V_{out} and i_{out} .

For mutual inductance identification, i_{in} and R_L are added to the mutual inductance identification algorithm to monitor whether the mutual inductance M has changed. Then, the identified M is used to obtain the optimal equivalent load $R_{\eta \max}$ through Equation (16), and the duty cycle D can be adjusted by combining Equation (16) and Equation (22). When D changes, V_{out} and the reference output voltage V_{ref} are compared, and the difference $e(t)$ between them is used to generate error information $u(t)$ through the PI controller. $u(t)$ along with D and M are transferred to the transmitting side of the system through wireless communication link. Finally, the inverter adjusts the phase shift angle θ based on the receiving circuit information, if V_{out} is greater than V_{ref} , increasing θ ; otherwise, reducing θ .

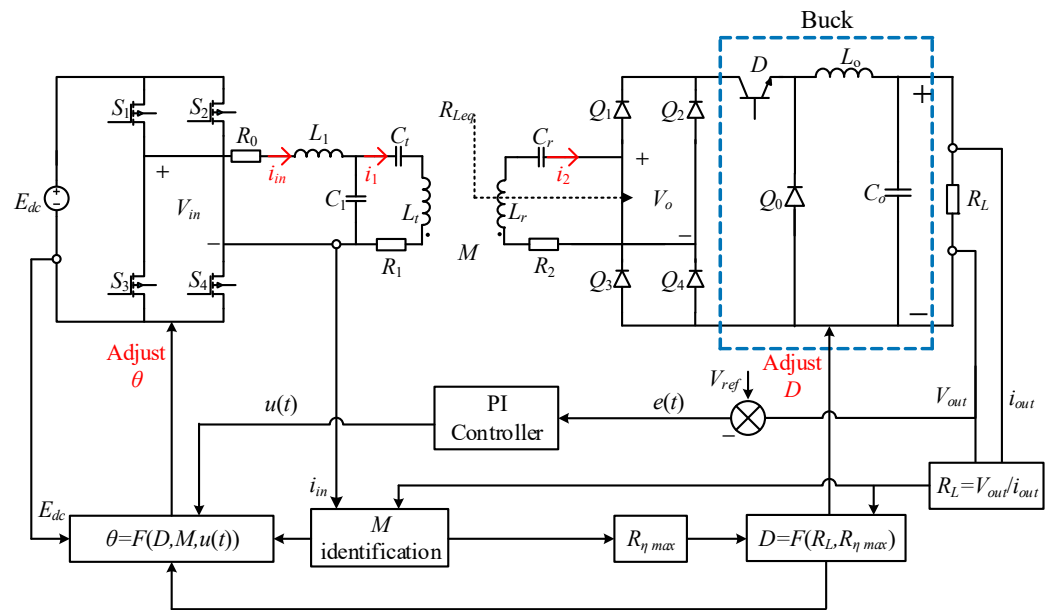


Figure 6. Strategy diagram of bilateral cooperation control strategy.

4. Simulation Analysis

In order to verify the accuracy improvement of GWO-PSO, MATLAB simulation was used for verification. Considering the resonance requirements of MCR-BE system, all parameters are set as Table 1.

Table 1. Parameter values of MCR-BE system.

Parameter	Value	Parameter	Value
E_{dc} (V)	310	L_s (μH)	158
L_1 (μH)	48.2	L_o (μH)	196
C_1 (nF)	13.2	C_o (nF)	1320
C_p (nF)	39.5	C_2 (nF)	470
C_s (nF)	4	M (μH)	35.5
L_p (μH)	64	R_L (Ω)	10

This article designs a WPT experimental device. The rated power is 200 W, the operating frequency f_0 is 200 kHz, the input voltage E_{dc} is 310 V, and the rated output voltage V_{out} is 48 V. The voltage acquisition circuit adopts the TL082 operational amplifier, the DSP control circuit adopts the TMS320F28035 chip, and the Bluetooth module adopts the CC2540 chip. All of them are produced by Texas Instruments (TI) in Dallas, TX, USA

In this paper, the transmitting and receiving coils are wound with Litz wire. The outer diameter of the transmitting coil is 26.5 cm, and the inner diameter is 20.5 cm. The “0.1 mm \times 200 strands” specification of the Litz wire wound into a planar disk spiral is used, and the number of turns is 12; the outer diameter of the receiving coil is 22.5 cm and the inner diameter is 10.5 cm. The “0.1 mm \times 150 strands” specification of the Litz wire wound into a planar disk spiral is used, and the number of turns is 28.

The coupling coil used in this article was wound with Litz wire and the inductance values of the two coils were measured using an LCR tester. After measurement, the inductance values of the two coils were 64 μH and 158 μH , respectively, and the parasitic resistances of the two coils were 0.075 Ω and 0.46 Ω , respectively. When the two coils were 0.8 cm apart, M was 35.5 μH .

According to the Litz wire manual, the maximum operating current of the Litz wire model with $0.102 \text{ mm} \times 162$ strands is 6.6 A. According to Equation (11) and f_0 , the minimum value of L_1 can be obtained as:

$$L_{1\min} = \frac{310 \text{ V}}{2\pi f_0 * 6.6\text{A}} = 37.38 \text{ } \mu\text{H} \quad (25)$$

The actual inductance value selected for L_1 is 48.2 μH .
 C_1 and L_1 are resonant; therefore, the value of C_1 is:

$$C_1 = \frac{1}{(2\pi f_0)^2 * L_1} = 13.19 \text{ nF} \quad (26)$$

The actual capacitance value of C_1 selected is 13.2 nF, which basically meets the design requirements of this article.

Resonance occurs between C_p , C_1 , and L_p ; therefore, the value of C_p is:

$$C_p = \frac{C_1}{(2\pi f_0)^2 * L_p C_1 - 1} = 39.52 \text{ nF} \quad (27)$$

The actual capacitance value of C_p selected is 39.5 nF, which meets the design requirements of this article.

Resonance occurs between C_s and L_s . Therefore, the value of C_s is:

$$C_s = \frac{1}{(2\pi f_0)^2 * L_s} = 4.01 \text{ nF} \quad (28)$$

The actual capacitance value of C_s selected is 4 nF, which meets the design requirements of this article.

When θ is 0, V_o can achieve the maximum value. First, calculate the maximum value of V_o :

$$V_o = \frac{MV_{in}}{L_1} = 229.27 \text{ V} \quad (29)$$

Therefore, the design specifications of the buck converter are as follows: the operating frequency f_1 is 100 kHz, the maximum input voltage V_o is 229.27 V, the rated output power P_{out} is 360 W, the rated output voltage V_{out} is 48 V, and the maximum output current i_{out} is 7.5 A.

The inductance L_o of a buck circuit is determined by the ripple rate of the inductor current. This article considers the relationship between the magnitude of ripple rate, inductance size, and output voltage ripple. A compromise is made by selecting a ripple rate of 0.27. Therefore, the ripple of the maximum inductance current is about 2 A, and the minimum value of L_o is 196 μH .

4.1. Identification Comparison between PSO and GWO-PSO

First, the two coils were set 0.8 cm apart and the load resistance was set to 20 Ω . A square wave signal with an amplitude of 310 V was selected to operate the WPT system model. After the system ran stably, the two inverter output currents one period apart were collected as test data and the data were input into PSO and GWO-PSO for iterative optimization. Then, the two algorithms were iteratively simulated, and the simulation results are shown in Figure 7.

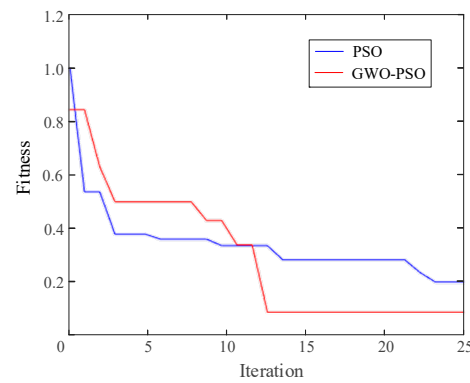


Figure 7. Iteration results of PSO and GWO-PSO.

From the iteration results, it can be seen that although GWO-PSO has a larger fitness function than conventional PSO in the initial stage, as the iteration number increases, GWO-PSO achieves smaller fitness values than conventional PSO after the 12th iteration. After the 13th iteration, GWO-PSO has become stable. This result indicates that GWO-PSO can not only achieve a more accurate mutual inductance identification result, but also a faster identification speed. In addition, GWO-PSO has the elite-group guidance strategy and surrounding-search strategy of GWO, which greatly improves the drawback of easily falling into a local optimum. The final mutual inductance identification value is 35.43 μH , with a relative error of 0.19% compared to the preset mutual inductance value, which meets the accuracy requirements of the system.

To further verify the effectiveness and accuracy of GWO-PSO, the load resistance R_L was changed based on a mutual inductance value of 35.5 μH , and identification was performed again. The results are shown in Table 2.

Table 2. Identification value of M under different load R_L (PSO and GWO-PSO).

Load Resistance/ Ω	PSO Mutual Inductance/ μH	Relative Error/%	GWO-PSO Mutual Inductance/ μH	Relative Error/%
15	35.03	1.32	34.99	1.44
20	35.80	0.85	35.70	0.56
25	35.16	0.96	35.22	0.79
30	36.09	1.66	36.00	1.41
35	34.73	2.17	34.82	1.92

According to the test results in Table 2, it can be found that within a certain range of load variations, the error of the identification results of PSO can reach a maximum of 2.17% and a minimum of 0.85%, whereas for the identification results of GWO-PSO, the error can be maintained within 2% and the minimum error can reach 0.56%. By comparison, it can be found that the overall identification accuracy of GWO-PSO is higher than that of PSO.

4.2. Bilateral Cooperation Control Strategy

Involving the bilateral cooperation control of the WPT system, this article designs a clock control module, which includes an impedance matching algorithm and PID control algorithm, respectively used to provide the drive signals for the buck converter and the full-bridge inverter. The drive signal for the buck converter is duty cycle D , while for the full-bridge inverter, the drive signal is phase shift angle θ . The drive signal of the inverter is 200 kHz, while for the buck converter, it is 100 kHz. Other circuit parameters are shown in Table 1.

When the mutual inductance is 24.72 μH and 35.5 μH , the input power P_{in} and output power P_{out} of the WPT system are shown in Figure 8. According to the impedance matching principle, the optimal equivalent load after rectification $R_{dc-\eta\max}$ (i.e., before the

buck converter) can be calculated as 95Ω and 136Ω , respectively. The duty cycle D is provided by the clock control module, and the phase shift angle θ is initialized to zero. The values of P_{in} and P_{out} at the optimal equivalent load $R_{dc-\eta_{max}}$ can be measured by removing the buck converter and directly connecting the load to the rectifier circuit, and the load can be set to 95Ω and 136Ω , respectively. The measured values of P_{in} and P_{out} are 270.2 W and 250.3 W under the mutual inductance of $24.72 \mu\text{H}$, and 388 W and 359.5 W under the mutual inductance of $35.5 \mu\text{H}$.

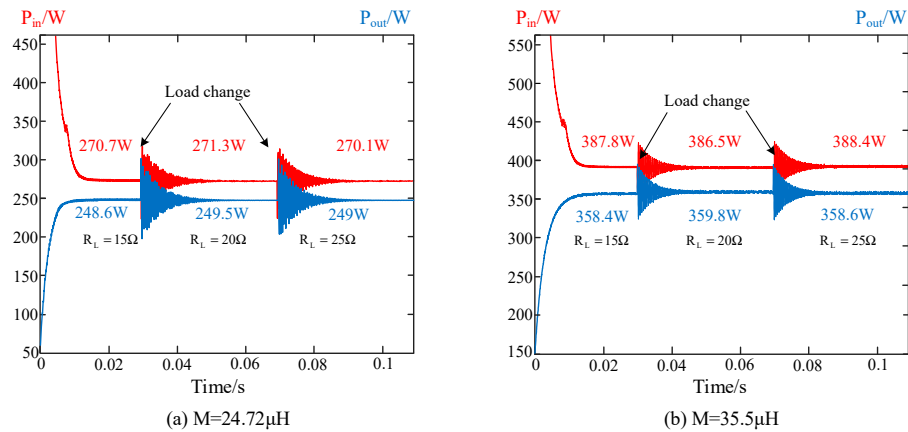


Figure 8. Impedance matching results under different mutual inductances: (a) $M = 24.72 \mu\text{H}$; (b) $M = 35.5 \mu\text{H}$.

After measuring the values of P_{in} and P_{out} , the buck converter can be connected after the rectifier to perform impedance matching. From Figure 8a (M is $24.72 \mu\text{H}$), it can be seen that when R_L is set to 15Ω , P_{in} and P_{out} stabilize at 270.7 W and 248.6 W , respectively. At 0.03 s , R_L switches from 15Ω to 20Ω , and P_{in} and P_{out} change to 271.3 W and 249.5 W after a brief oscillation. Compared with P_{in} and P_{out} before the load switched, the relative errors are 0.22% and 0.36% , respectively. Similarly, at 0.07 s , when R_L switches from 20Ω to 25Ω , P_{in} and P_{out} become 270.1 W and 249 W . Compared with P_{in} and P_{out} before the load switched, the relative errors are 0.22% and 0.16% , respectively.

Similarly, the impedance matching situation of $35.5 \mu\text{H}$ is shown in Figure 8b, and the operation steps and principles are the same as those in Figure 8a. Based on the above simulation results, it can be concluded that when the load is randomly switched within a certain range, using a buck converter for impedance matching can maintain a relatively high transmission efficiency of the WPT system. When the mutual inductance changes, the variation can be accurately identified through GWO-PSO, and then impedance matching can be performed.

When R_L and M change, the optimal equivalent load after the rectifier $R_{dc-\eta_{max}}$ can be calculated based on the identification mutual inductance; then, P_{in} and P_{out} of the WPT system can be measured at this time. Finally, the duty cycle D can be controlled by the clock signal for impedance matching, so that the WPT system can maintain a high transmission efficiency within a certain range of load variation. According to Equation (23), when the mutual inductance M and duty cycle D change, the output voltage V_{out} will also change. Therefore, based on the maximum efficiency optimization, the system can achieve constant voltage output through phase shift modulation. Figure 9 shows the waveform of the output voltage V_{out} after phase shift modulation under different mutual inductance conditions

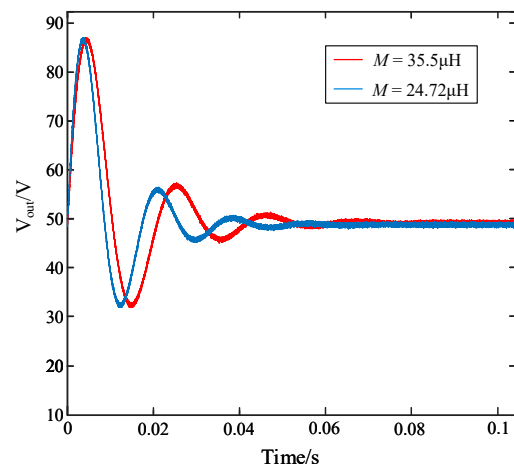


Figure 9. Output voltage of the WPT system under different mutual inductance values.

From the simulation results, it can be seen that after phase shift modulation, V_{out} can be basically stable at around 48V after a brief output fluctuation (about 0.06s), allowing the system to maintain constant voltage output. In addition, for cases with different M (taking 35.5 μ H and 24.72 μ H as examples), V_{out} can be also maintained at around 48V after 0.06s. This indicates that even if M and R_L undergo uncertain changes, the system can still directly change V_{out} through adjusting θ .

5. Experiment Verification

Based on the control framework designed in Section 4, an experimental platform was built, and the component parameters of the WPT system are shown in Table 1. The specific experimental equipment is shown in Figure 10. The experiment maintained a DC input voltage of 310 V and a reference output voltage of 48 V throughout the experiment. All resonant slots of the WPT system were in resonance state. Due to the limitations of the experimental equipment, the WPT system equipment was used for the experimental verification of MCR-BE system in this article.

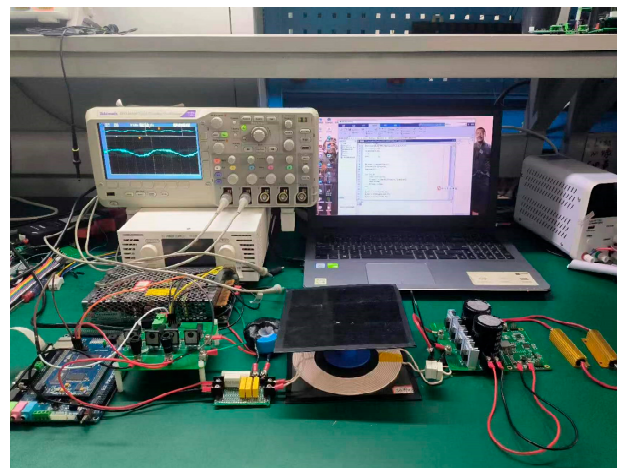


Figure 10. Experiment equipment of the WPT system

5.1. Experiment of Mutual Inductance Identification

Considering that the experiment tends to be more practical, the lateral offset of the coupling coils was added during the experiment, and the mutual inductance was measured during the lateral offset of the receiving coil. According to the verification in Section 4, the influence of load variation on the identification accuracy can be ignored within a certain range, and considering the feasibility of the experiment, the load resistance was fixed at

20 Ω . The transmission distance between the transmitting coil and the receiving coil was kept at 8 cm, and the mutual inductance was experimentally tested when the offset distance was 1 cm, 2 cm, 3 cm, 4 cm, 5 cm, 6 cm, and 7 cm. The comparison between the experimentally measured mutual inductance values and GWO-PSO identified mutual inductance values is shown in Table 3.

Table 3. Identification values and experimental values of M under offset variations.

Offset Distance/cm	Experimental Mutual Inductance/ μH	Identification Mutual Inductance/ μH	Relative Error/%
1	31.74	33.12	4.35
2	29.06	30.25	4.09
3	25.90	27.14	4.79
4	22.53	23.58	4.66
5	18.61	19.36	4.03
6	13.72	14.40	4.96
7	8.43	8.88	5.34

From the comparison results in Table 3, it can be seen that when the lateral offset distance is within 7 cm, the relative error between the experimental value and the identification value can be kept within 5%, with a minimum of 4.03%. The error is mainly due to the difficulty of achieving the ideal state in the experimental process; in addition, the experiment neglects parasitic parameters of some components. Secondly, inevitable interference will occur during the sampling process, which will result in lower identification accuracy in the experiment than in the simulation. Finally, since the WPT system transfers energy through electromagnetic coupling, there will be an unpredictable leakage magnetic field, which also presents significant differences between the experiment and the simulation. After excluding the above error factors, it can be seen from the experimental results that GWO-PSO can accurately identify the mutual inductance under the condition of lateral offset, which lays the foundation for bilateral cooperation control experiments. Figure 11 shows the deviation between identification values and experimental values of mutual inductance M under different offset distances, and red triangles in Figure 11 represents the error rate between identification values and experimental values of M .

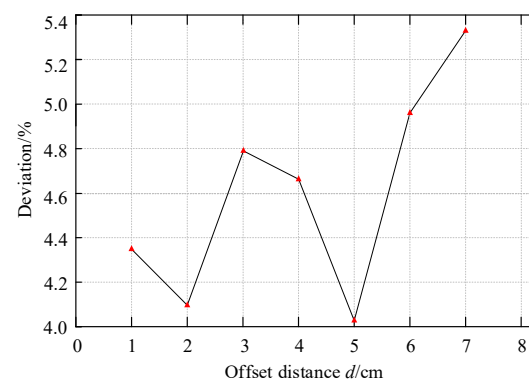


Figure 11. Deviation between identification values and experimental values of mutual inductance under offset variations.

5.2. Experiment of Bilateral Cooperation Control Strategy

In order to verify the control effect of the bilateral cooperation control strategy, with the receiving coil positioned 8 cm away from the transmitting coil, the output results were compared under different loads R_L (15 Ω , 20 Ω , and 25 Ω) and different lateral offset distances d (1 cm, 3 cm, and 5 cm). Then, the bilateral cooperation control algorithm was implemented. Figure 12 shows the experimental results. From the experimental results, it can be observed that when R_L remains constant and d increases, D also increases. The

reason for this is that as the mutual inductance M decreases, the optimal equivalent load $R_{\eta_{max}}$ becomes smaller, and D automatically follows the corresponding $R_{\eta_{max}}$. Meanwhile, because d becomes larger, the output voltage V_{out} decreases. In order to achieve a constant voltage output, the phase shift angle θ will decrease. From three sets of horizontal comparative experiments (a~c, d~f, g~i), it can be observed that V_{out} can stabilize at 48 V.

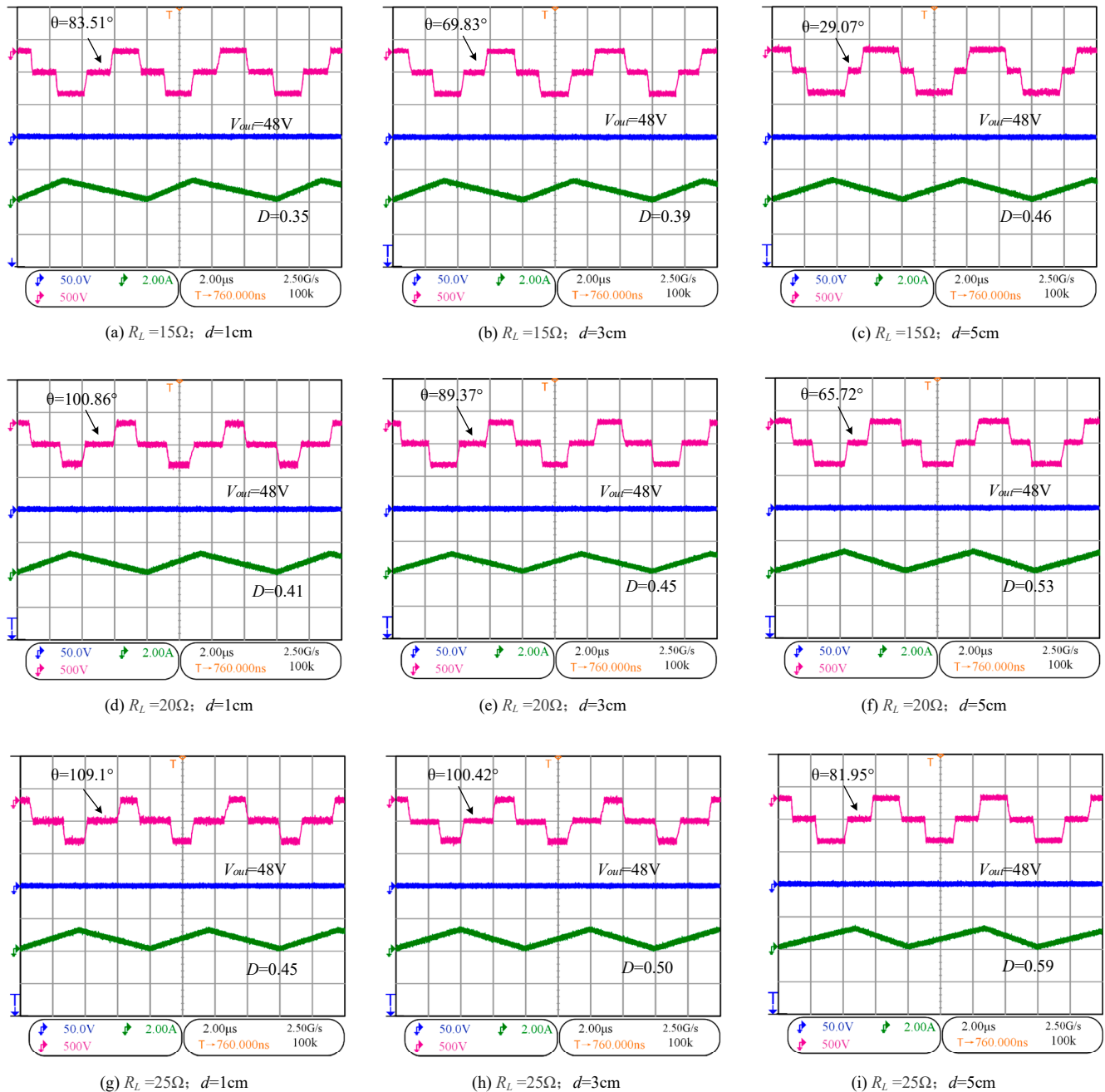


Figure 12. Control effects of the bilateral cooperation control algorithm.

From the experimental results, it can also be seen that when d remains constant and R_L gradually increases, the duty cycle D will increase accordingly, which is the result of impedance matching. At the same time, the duty cycle D increases and the mutual inductance M maintains constant. In order to achieve constant voltage output, θ will increase. From three sets of vertical comparative experiments (a~g, b~h, c~i), it can be observed that V_{out} can stabilize at 48 V.

Figure 12 shows the changes in D and θ under the bilateral cooperation control strategy. In order to verify whether the strategy has achieved the goal of maximum efficiency optimization, it is also necessary to verify whether the transmission efficiency corresponding to the three different scenarios meets the requirements under different values of d . Figure 13 shows the transmission efficiency under three different scenarios.

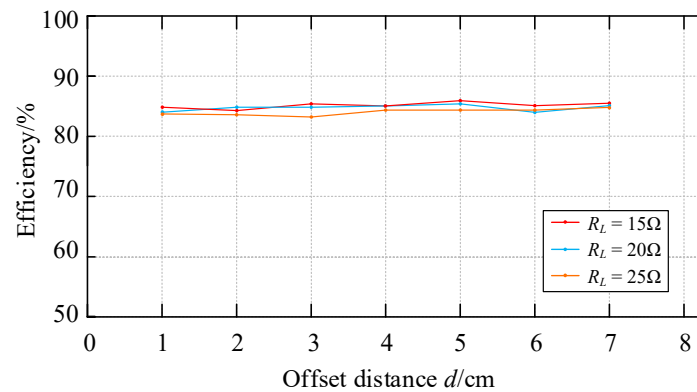


Figure 13. Transmission efficiency under different offset distances and loads.

From Figure 13, it can be seen that when the load is 15Ω , η_{max} can reach 86%, with a minimum of 84% and a fluctuation rate of 2%; when the load is 20Ω , η_{max} can reach 85.5%, the minimum is 83.5%, and the fluctuation rate is 2%; when the load is 25Ω , η_{max} can reach 85%, the minimum is 83%, and the fluctuation rate is 2%. From the three sets of experimental results, it can be seen that the transmission efficiency can be maintained at around 84.5%. The above experiments ultimately prove that under the condition of changing load and mutual inductance, the bilateral cooperation control strategy can achieve maximum efficiency optimization and constant voltage output, with the output voltage finally stabilizing at 48 V and the transmission efficiency being basically maintained at 84.5%.

6. Conclusions

Electric excitation synchronous motors require a brush and slip ring during the excitation process. In response to the adverse effects caused by the brush and slip ring, this article proposes a novel brushless excitation system named MCR-BE system. The excitation system consists of a wireless charging system and a motor, both of which are based on WPT system. The DC power supply transmits electrical energy to the battery through the wireless charging system, and then the battery transmits the electrical energy to the motor. Through the magnetic coupling between the stator and rotor, the electrical energy is transmitted from the stator to the rotor, driving the motor to operate. During the entire operation, the motor does not require a brush and slip ring, thus achieving brushless excitation. The main work achieved in this article is as follows:

- (1) Aiming at the problem of coupling coil offset in wireless charging systems, an improved particle swarm optimization algorithm GWO-PSO is proposed for mutual inductance identification, and the GWO-PSO algorithm is compared with the PSO algorithm. Through simulation and experimental results, it can be seen that the PSO identification under the condition of fixed mutual inductance and load variation can reach a minimum identification error rate of 0.85% and a maximum error rate of 2.17%. The GWO-PSO identification can reach a minimum identification error rate of 0.56% and a maximum error rate of 1.92%. Therefore, the GWO-PSO algorithm has improved identification accuracy. In the experimental process, we also conducted mutual inductance identification under the condition of mutual inductance variation, and the result showed that the identification error rate can reach a minimum identification error rate of 4.03% and a maximum error rate of 5.34%, which was higher

than the identification accuracy under the condition of constant mutual inductance. Therefore, further improvement in the GWO-PSO algorithm is needed to improve the recognition accuracy.

- (2) This article proposes a bilateral cooperation control strategy to deal with the simultaneous changes in load and mutual inductance in wireless charging systems, aiming to maintain maximum transmission efficiency while maintaining constant voltage output. By impedance matching of the buck converter on the receiving side of the system, the equivalent load can track the optimal equivalent load, thereby achieving maximum transmission efficiency. The receiving side transmits circuit information such as the duty cycle and mutual inductance to the primary side through wireless communication links. Then, the transmitting side uses PID control to adjust the inverter through PSM to maintain constant voltage output. According to simulation and experimental results, the output voltage of the system can be maintained at around 48 V, while the transmission efficiency can be maintained at around 84.5%.
- (3) Due to the limitations of the experimental equipment, this work did not incorporate wireless energy transmission systems into wireless charging systems and motors. Instead, it simulated the mutual inductance and load changes between coupling coils, and proposed a bilateral cooperation control strategy to track the maximum transmission efficiency and maintain a constant voltage output of the system. Therefore, we will strive to develop a complete brushless excitation system in the future and apply the control strategy to actual experimental equipment.

Author Contributions: Conceptualization, K.L. and Y.L.; methodology, K.L.; software, K.L. and X.T.; validation, K.L., Y.L. and X.S.; formal analysis, K.L.; investigation, K.L.; resources, K.L.; data curation, K.L.; writing—original draft preparation, K.L. and Y.L.; writing—review and editing, Y.L. and X.T.; visualization, K.L.; supervision, K.L. and X.S.; project administration, K.L. and X.S.; funding acquisition, K.L. and X.S. All authors have read and agreed to the published version of the manuscript.

Funding: This research was funded by the National Natural Science Foundation of China under Project 52002155.

Data Availability Statement: The original contributions presented in the study are included in the article, further inquiries can be directed to the corresponding author.

Conflicts of Interest: The authors declare no conflicts of interest.

Abbreviations

MCR-BE	Magnetic coupling resonant brushless excitation
PMSM	Permanent magnet synchronous motor
EESM	Electrically excited synchronous motor
WPT	Wireless power transfer
PSO	Particle swarm optimization
GWO-PSO	Grey wolf optimization–particle swarm optimization
M	Mutual inductance
R_L	Load
R_{Leq}	Equivalent load
$R_{\eta max}$	Optimal equivalent load
D	Duty cycle
θ	Phase shift angle
E_{dc}	DC input power supply
V_{in}	Inverter output voltage
i_{in}	Inverter output current
i_1	Transmitting current
i_2	Receiving current
V_o	Equivalent output voltage
V_{out}	Load voltage

P_{in}	Input power
P_{out}	Output power
η	Transmission efficiency
η_{max}	Maximum transmission efficiency

References

- Madawala, U.K.; Thrimawithana, D.J. A bidirectional inductive power interface for electric vehicles in V2G systems. *IEEE Trans. Ind. Electron.* **2011**, *58*, 4789–4796. [\[CrossRef\]](#)
- Sun, X.; Zhang, Y.; Lei, G.; Guo, Y.; Zhu, J. An improved deadbeat predictive stator flux control with reduced-order disturbance observer for in-wheel PMSMs. *IEEE/ASME Trans. Mechatron.* **2021**, *27*, 690–700. [\[CrossRef\]](#)
- Sun, X.; Li, T.; Tian, X.; Zhu, J. Fault-tolerant operation of a six-phase permanent magnet synchronous hub motor based on model predictive current control with virtual voltage vectors. *IEEE Trans. Energy Convers.* **2021**, *37*, 337–346. [\[CrossRef\]](#)
- Sun, L.; Liu, M.; Wang, Z.; Wang, C.; Luo, F. Research on Load Spectrum Reconstruction Method of Exhaust System Mounting Bracket of a Hybrid Tractor Based on MOPSO-Wavelet Decomposition Technique. *Agriculture* **2023**, *13*, 1919. [\[CrossRef\]](#)
- Jin, Z.; Sun, X.; Cai, Y.; Tian, X. Robust Collaborative Optimization Design of Plug-in Hybrid Electric Bus Based on 6 Sigma Theory. *IEEE Trans. Transp. Electrification* **2024**. [\[CrossRef\]](#)
- Jin, Z.; Sun, X.; Lei, G.; Guo, Y.; Zhu, J. Sliding mode direct torque control of SPMSMs based on a hybrid wolf optimization algorithm. *IEEE Trans. Ind. Electron.* **2021**, *69*, 4534–4544. [\[CrossRef\]](#)
- Sun, X.; Su, Z.; Lei, G.; Cai, Y.; Yao, M. Adaptive Model-Free Predictive Current Control for SPMSM Drives With Optimal Virtual Vector Modulation. *IEEE/ASME Trans. Mechatron.* **2023**. [\[CrossRef\]](#)
- Chu, W.; Zhu, Z.-Q.; Chen, J. Simplified analytical optimization and comparison of torque densities between electrically excited and permanent-magnet machines. *IEEE Trans. Ind. Electron.* **2013**, *61*, 5000–5011. [\[CrossRef\]](#)
- Wang, L.; Li, J.; Nie, H.; Liu, J.; Ke, S. Coaxial nested couplers-based offset-tolerance rotary wireless power transfer systems for electric excitation motors. *IEEE Access* **2020**, *8*, 44913–44923. [\[CrossRef\]](#)
- Kou, J.; Gao, Q.; Sha, Z.; Teng, Y.; Xu, D. A rotor position detection method at high speed for electrically excited synchronous motor. In Proceedings of the 2019 22nd International Conference on Electrical Machines and Systems (ICEMS), Harbin, China, 11–14 August 2019; pp. 1–5.
- Veitengruber, J. Design and characterization of a cost-effective and high-power density brushless rotor supply for mobile synchronous generators. In Proceedings of the 2015 International Conference on Sustainable Mobility Applications, Renewables and Technology (SMART), Kuwait City, Kuwait, 23–25 November 2015; pp. 1–6.
- Li, W.; Mei, W.; Yuan, Q.; Song, Y.; Dongye, Z.; Diao, L. Detuned resonant capacitors selection for improved misalignment tolerance of LCC-S compensated wireless power transfer system. *IEEE Access* **2022**, *10*, 49474–49484. [\[CrossRef\]](#)
- Zhou, F.; Huang, D.; Wang, F. A particle swarm optimization parameter identification algorithm based on model predictive control of wireless power transfer system. In Proceedings of the 2019 IEEE 3rd Advanced Information Management, Communicates, Electronic and Automation Control Conference (IMCEC), Chongqing, China, 11–13 October 2019; pp. 391–396.
- Yu, Y.; Wang, X. Characteristic analysis of relatively high speed, loosely coupled rotating excitation transformers in HEV and EV drive motor excitation systems. *IEICE Electron. Express* **2017**, *14*, 20161218. [\[CrossRef\]](#)
- Nozawa, R.; Kobayashi, R.; Tanifuji, H.; Kaneko, Y.; Abe, S. Excitation system by contactless power transfer system with the primary series capacitor method. In Proceedings of the 2014 International Power Electronics Conference (IPEC-Hiroshima 2014-ECCE ASIA), Hiroshima, Japan, 18–21 May 2014; pp. 1115–1121.
- Raminosoa, T.; Wiles, R.H.; Wilkins, J. Novel rotary transformer topology with improved power transfer capability for high-speed applications. *IEEE Trans. Ind. Appl.* **2019**, *56*, 277–286. [\[CrossRef\]](#)
- Yao, Y.; Wang, Y.; Liu, X.; Lin, F.; Xu, D. A novel parameter tuning method for a double-sided LCL compensated WPT system with better comprehensive performance. *IEEE Trans. Power Electron.* **2017**, *33*, 8525–8536. [\[CrossRef\]](#)
- Zhang, Y.; Guo, Y.; Wang, L.; Bo, Q.; Liu, Z. An Optimization Method of Dual-Side LCC Compensation Networks Simultaneously Considering Output Power and Transmission Efficiency in Two Directions for BWPT Systems. *IEEE J. Emerg. Sel. Top. Ind. Electron.* **2022**, *3*, 500–508. [\[CrossRef\]](#)
- Zhang, Y.; Liu, R.; Wang, H.; Mao, X.; Chen, X. Current Balancing of a Multiphase Inverter for LCC-S Compensated Wireless Power Transfer System Based on Mutually Negatively Coupled Inductors. *IEEE Trans. Power Electron.* **2023**, *38*, 12411–12415. [\[CrossRef\]](#)
- Deng, C.; Deng, Q.; Liu, W.; Yu, C.; Hu, J.; Li, X. Analysis of vibration and noise for the powertrain system of electric vehicles under speed-varying operating conditions. *Math. Probl. Eng.* **2020**, *2020*, 1–9. [\[CrossRef\]](#)
- Chen, J.-W. Accurate modeling and analysis of the winding inductances of a linear permanent-magnet actuator using an improved Fourier series expansion. *Int. J. Appl. Electromagn. Mech.* **2021**, *66*, 297–312. [\[CrossRef\]](#)
- Liu, C.; Zhang, B.; Hu, Y.; Cao, B.; Han, W. Maximum Efficiency Tracking of Wireless Power Transfer by Using Receiver-Side Variable Capacitors. In Proceedings of the IECON 2023-49th Annual Conference of the IEEE Industrial Electronics Society, Singapore, 16–19 October 2023; pp. 1–6.
- Zhong, W.X.; Hui, S. Maximum energy efficiency tracking for wireless power transfer systems. *IEEE Trans. Power Electron.* **2014**, *30*, 4025–4034. [\[CrossRef\]](#)

24. Fu, M.; Yin, H.; Zhu, X.; Ma, C. Analysis and tracking of optimal load in wireless power transfer systems. *IEEE Trans. Power Electron.* **2014**, *30*, 3952–3963. [[CrossRef](#)]
25. Yeo, T.-D.; Kwon, D.; Khang, S.-T.; Yu, J.-W. Design of maximum efficiency tracking control scheme for closed-loop wireless power charging system employing series resonant tank. *IEEE Trans. Power Electron.* **2016**, *32*, 471–478. [[CrossRef](#)]
26. Li, Z.; Song, K.; Jiang, J.; Zhu, C. Constant current charging and maximum efficiency tracking control scheme for supercapacitor wireless charging. *IEEE Trans. Power Electron.* **2018**, *33*, 9088–9100. [[CrossRef](#)]
27. Song, K.; Wei, R.; Yang, G.; Zhang, H.; Li, Z.; Huang, X.; Jiang, J.; Zhu, C.; Du, Z. Constant current charging and maximum system efficiency tracking for wireless charging systems employing dual-side control. *IEEE Trans. Ind. Appl.* **2019**, *56*, 622–634. [[CrossRef](#)]
28. Yin, J.; Lin, D.; Parisini, T.; Hui, S. Front-end monitoring of the mutual inductance and load resistance in a series–series compensated wireless power transfer system. *IEEE Trans. Power Electron.* **2015**, *31*, 7339–7352. [[CrossRef](#)]
29. Sheng, X.; Shi, L. Mutual inductance and load identification method for inductively coupled power transfer system based on auxiliary inverter. *IEEE Trans. Veh. Technol.* **2019**, *69*, 1533–1541. [[CrossRef](#)]
30. Tian, Y.; Zhu, Z.; Xiang, L.; Tian, J. Vision-based rapid power control for a dynamic wireless power transfer system of electric vehicles. *IEEE Access* **2020**, *8*, 78764–78778. [[CrossRef](#)]
31. Huang, Z.; Qin, T.; Li, X.L.; Ding, L.; Iu, H.H.-C.; Chi, K.T. Synthesis of Inductive Power Transfer Converters with Dual Imittance Networks for Inherent CC-to-CV Charging Profiles. *IEEE Trans. Power Electron.* **2024**, *39*, 7766–7777. [[CrossRef](#)]
32. Chen, J.; Yu, C.W.; Cheng, R.-H. Collaborative hybrid charging scheduling in wireless rechargeable sensor networks. *IEEE Trans. Veh. Technol.* **2022**, *71*, 8994–9010. [[CrossRef](#)]
33. Huang, Y.; Shinohara, N.; Mitani, T. Impedance matching in wireless power transfer. *IEEE Trans. Microw. Theory Tech.* **2016**, *65*, 582–590. [[CrossRef](#)]
34. Jiang, H.; Xu, W.; Chen, Q. Evaluating aroma quality of black tea by an olfactory visualization system: Selection of feature sensor using particle swarm optimization. *Food Res. Int.* **2019**, *126*, 108605. [[CrossRef](#)]
35. Chen, Y.; Chen, L.; Huang, C.; Lu, Y.; Wang, C. A dynamic tire model based on HPSO-SVM. *Int. J. Agric. Biol. Eng.* **2019**, *12*, 36–41. [[CrossRef](#)]
36. Sun, X.; Xiong, Y.; Yao, M.; Tang, X.; Tian, X. A unified control method combined with improved TSF and LADRC for SRMs using modified grey wolf optimization algorithm. *ISA Trans.* **2022**, *131*, 662–671. [[CrossRef](#)] [[PubMed](#)]
37. Sun, X.; Zhang, Y.; Tian, X.; Cao, J.; Zhu, J. Speed sensorless control for IPMSMs using a modified MRAS with gray wolf optimization algorithm. *IEEE Trans. Transp. Electrif.* **2021**, *8*, 1326–1337. [[CrossRef](#)]
38. Song, K.; Li, Z.; Jiang, J.; Zhu, C. Constant current/voltage charging operation for series–series and series–parallel compensated wireless power transfer systems employing primary-side controller. *IEEE Trans. Power Electron.* **2017**, *33*, 8065–8080. [[CrossRef](#)]

Disclaimer/Publisher’s Note: The statements, opinions and data contained in all publications are solely those of the individual author(s) and contributor(s) and not of MDPI and/or the editor(s). MDPI and/or the editor(s) disclaim responsibility for any injury to people or property resulting from any ideas, methods, instructions or products referred to in the content.